As noted by Neelin (2007), it is common to assume that $D\Phi/Dt \simeq \omega\partial_p\Phi$ to obtain Eq. (2), rather than using Eq. (9) (Emanuel et al. 1994; see section 4 of Betts 1974). As we will see below, this assumption is erroneous at the large scale since $\partial_t\Phi$ and $\mathbf{v}\cdot\nabla_h\Phi$ are not always negligibly small. We also show in appendix B that these terms make the DSE budget inaccurate.

We can eliminate $\mathbf{v}\cdot\nabla_h\Phi$ from Eq. (10) by invoking the kinetic energy budget, which is obtained by taking the dot product of the terms in Eq. (3a) and $\mathbf{v}$. This procedure eliminates the Coriolis force. Furthermore, as in Bister and Emanuel (1998), and Randall (2015), we make the following expansion:

$$\mathbf{v}\cdot\frac{\partial\overline{\omega'\mathbf{v}'}}{\partial p} = \frac{\partial\mathbf{v}\cdot\overline{\omega'\mathbf{v}'}}{\partial p} - \overline{\omega'\mathbf{v}'}\cdot\frac{\partial\mathbf{v}}{\partial p}. \tag{11}$$

Let us assume that the smaller-scale vertical flux of horizontal momentum is predominantly downgradient so that $\overline{\omega'\mathbf{v}'} \simeq -\mu\partial_p\mathbf{v}$, where μ is the eddy transfer coefficient. By doing this, we can write Eq. (11) as

$$-\mathbf{v}\cdot\frac{\partial\overline{\omega'\mathbf{v}'}}{\partial p} = \mu\frac{\partial^2 K}{\partial p^2} - \underbrace{\mu\left(\frac{\partial K}{\partial p}\right)^2}_{\mathcal{D}}, \tag{12}$$

where

$$K = \frac{1}{2}(u^2 + v^2) \tag{13}$$

is the kinetic energy per unit mass.

It is worth pointing out that squall lines and other forms of organized convection can transport kinetic energy upgradient (LeMone et al. 1984; Moncrieff and Klinker 1997). Hence, caution should be exercised when interpreting the scaling of these terms when these types of systems are present.

By examining Eq. (12) we see that the first term on the rhs is a vertical diffusion of K, which can be either positive or negative depending on how K is vertically distributed. On the other hand, the second term ($\mathcal{D}$) is always negative and acts to dissipate K. The dissipated K turns into heat, hence why it shows up in Eq. (3d).

By applying Eq. (12), the resulting K budget is written as

$$\frac{DK}{Dt} = -\mathbf{v}\cdot\nabla_h\Phi + \mu\frac{\partial^2 K}{\partial p^2} - \mathcal{D}. \tag{14}$$

Adding Eqs. (10) and (14) yields what we will refer to as the "moist nonstatic energy equation":

$$\frac{DE_m}{Dt} = \frac{\partial\Phi}{\partial t} + Q_r - \frac{\partial\overline{\omega'm'}}{\partial p} + \mu\frac{\partial^2 K}{\partial p^2}, \tag{15}$$

where

$$E_m = m + K \tag{16}$$

is the moist nonstatic energy, not to be confused with the mechanical energy (Randall 2015).

To simplify the turbulent fluxes in Eq. (15), many researchers choose to invoke the column-integrated MSE budget rather than its vertically resolved form. The mass-weighted vertical integral of E_m is written as

$$\langle E_m\rangle = \frac{1}{g}\int_0^{p_s} E_m\,dp, \tag{17}$$

where $p_s = 1000$ hPa is the surface pressure. The angle brackets denote a mass-weighted vertical integral over the atmospheric column. After column integration, we write the E_m budget as

$$\frac{\partial\langle E_m\rangle}{\partial t} = \frac{\partial\langle\Phi\rangle}{\partial t} - \nabla_h\cdot\langle\mathbf{v}E_m\rangle + \langle Q_r\rangle + L_vE + H - F_K, \tag{18}$$

where E is the surface evaporation rate, H is the surface sensible heat flux, and

$$F_K = -\left\langle\mu\frac{\partial^2 K}{\partial p^2}\right\rangle = C_d\rho_s|\mathbf{v}_s|^3 \tag{19}$$

is the surface K flux, where C_d is a bulk surface drag coefficient, and ρ_s is the surface density. Further details on how to obtain Eq. (18) from Eq. (15) are shown in appendix A. An alternate form of Eq. (18) is shown in appendix C

For the MSE budget in Eq. (2) to be derived as an approximation of Eq. (15) or Eq. (18), the following conditions must be satisfied:

1) Condition 1: The column integrated tendency in geopotential must be much smaller in amplitude than the MSE tendency, i.e., $|\partial_t\Phi| \ll |\partial_t m|$.
2) Condition 2: Temporal and spatial fluctuations in K must be much smaller than those in MSE.
3) Condition 3: The surface kinetic energy flux (F_K) must be negligibly small.

It is important to note that while m is on the order of 10^5 J kg^{-1}, its fluctuations are on the order of 10^3 J kg^{-1} (Adames et al. 2021). On the other hand, K fluctuations range from 1 J kg^{-1} in some equatorial waves, up to 10^3 J kg^{-1} in mature TCs. Furthermore, because the column integral of Φ is equivalent to that of R_dT (appendix C), it follows that Φ fluctuations are roughly $R_d/(C_p + R_d) \approx 0.22$ those of DSE. Thus, $\partial_t\Phi$ could potentially be nonnegligible in Eq. (15). A more careful examination of the relative magnitude of the terms in Eq. (15) is warranted.

3. Scale analysis

We will now perform a scale analysis on Eq. (15) in order to understand when the MSE budget is an accurate approximation of Eq. (15). As in Adames (2022), we begin by creating nondimensional versions of Eqs. (3a)–(3e). This section will focus on nongeostrophic scaling in the momentum equations. See Table 2 for a list of the scales, along with their definitions, and units; note that all scales, except lowercase Greek letters, are shown in straight font. Results for geostrophic scaling are shown in appendix D.

The NSA was defined by the following locations: Gan Island (0.69°N, 73.51°E), R/V *Revelle* (0°, 80.5°E), Colombo (6.91°N, 79.878°E), and Malé (4.91°N, 73.53°E). The sounding array dataset was quality controlled and bias corrected to produce DYNAMO NSA (version 3a) legacy dataset (Ciesielski et al. 2014). Precipitation is obtained from the 3B42 dataset of the Tropical Rainfall Measuring Mission (TRMM) (Huffman et al. 2007). The TRMM data are averaged over the NSA DYNAMO domain to produce a rainfall time series.

Three-dimensional fields including zonal (u) and meridional (v) winds, geopotential (Φ), temperature (T), and specific humidity (q) are obtained from the fifth generation of the European Centre for Medium-Range Weather Forecasts (ECMWF) reanalysis (ERA5; Hersbach et al. 2019). We use ERA data from January 1980 through December 2015. In addition, the MJO activity during the DYNAMO period is assessed through the OLR MJO index (OMI; Kiladis et al. 2014).

The power spectrum calculation procedure is similar to previous studies (e.g., Wheeler and Kiladis 1999; Yasunaga et al. 2019; Inoue et al. 2020). All terms are first partitioned into symmetric and antisymmetric components over the 10°S–10°N latitude belt. To prevent aliasing, the first three harmonics of the seasonal cycle are removed. Anomalies were partitioned into 96-day segments, as in Wheeler and Kiladis (1999). Then for each segment, the linear trend is removed, and the ends of the series are tapered to zero. Finally, the power spectra were computed.

The amplitudes of the terms relative to the column-integrated MSE anomalies and the MSE tendency are examined via the aforementioned spectral analysis. We use the square root of the individual power spectra:

$$\mathcal{R}(\langle K\rangle, \langle m\rangle) = \sqrt{\mathcal{P}(\langle K\rangle)/\mathcal{P}(\langle m\rangle)}, \tag{39}$$

where $\mathcal{P}$ is the power spectrum, and angle brackets denote a mass-weighted integral from the surface to the top of the atmosphere. We use this method rather than the ratio of the cospectrum and the power spectrum used by Yasunaga et al. (2019) and Inoue et al. (2020) because we are mainly interested in the relative amplitude between the terms, not in their covariance. However, the results are not sensitive to the method used.

b. Comparison with observations and reanalysis

In Fig. 1 we see that the column geopotential tendency ($\partial_t\langle\Phi\rangle$) is roughly an order of magnitude smaller than $\partial_t\langle m\rangle$, while $\partial_t\langle K\rangle$ is roughly two orders of magnitude smaller. These two terms remain relatively flat in increasing frequency. In contrast, F_K is roughly three orders of magnitude smaller than $\partial_t\langle m\rangle$ at time scales longer than 10 days. It decreases in amplitude with increasing frequency, consistent with the scaling shown in Eq. (37). Interestingly, F_K starts increasing with frequency at subdiurnal time scales, perhaps because of the influence of convection or boundary layer processes. Overall, Fig. 1 shows that the three conditions discussed above are satisfied at most frequencies in the DYNAMO NSA data. Furthermore, we see that $\partial_t L_v\langle q\rangle$ is on the same order as $\partial_t\langle m\rangle$, consistent with the idea that moisture must account for a large fraction of the MSE variance for the MSE budget to be accurate.

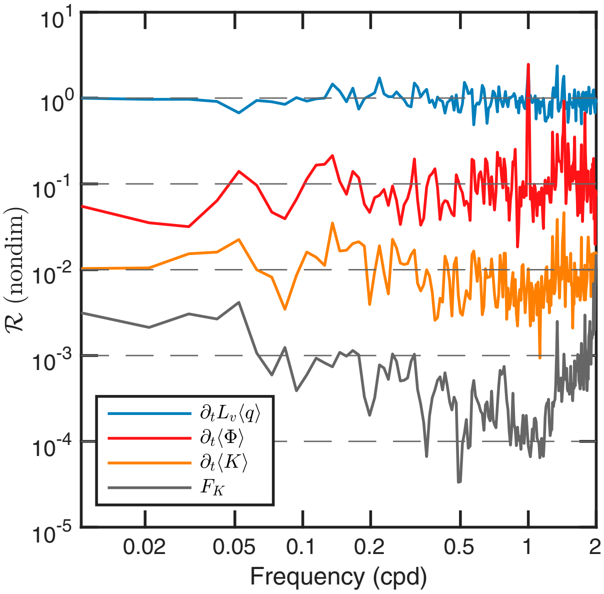

FIG. 1. Square root of the ratios of the power spectra ($\mathcal{R}$) as obtained from Eq. (39): $\mathcal{R}(L_v\partial_t\langle q\rangle, \partial_t\langle m\rangle)$ (blue), $\mathcal{R}(\partial_t\langle\Phi\rangle, \partial_t\langle m\rangle)$ (red), $\mathcal{R}(\partial_t\langle K\rangle, \partial_t\langle m\rangle)$ (orange), and $\mathcal{R}(F_K, \partial_t\langle m\rangle)$ (gray). The data used are from DYNAMO's northern sounding array. Note that both axes are on a logarithmic scale.

The fractional quantities of the terms relative to the MSE anomalies in ERA5 data are also shown as a function of zonal wavenumbers and temporal frequencies (Fig. 2). From examination of Fig. 2 we see that K is roughly 1/100 to 1/30 times the amplitude of $\langle m\rangle$, consistent with the analysis done on the DYNAMO NSA data in Fig. 1. However, we see variability in the wavenumber–frequency space that is not seen in the more limited analysis presented in Fig. 1. For example, we see a large $\mathcal{R}(\langle K\rangle, \langle m\rangle)$ along the dispersion curve of Kelvin waves with equivalent depths greater than 90 m (Fig. 2a). We also see a reduction in $\mathcal{R}(\langle K\rangle, \langle m\rangle)$ with decreasing spatial scales (increasing magnitude of the zonal wavenumber).

When we examine the relative amplitude of $\langle\Phi\rangle$ with respect to $\langle m\rangle$ (Figs. 2c,d), we see that there is a region where the magnitude exceeds 0.2 near westward-propagating zonal wavenumber 1 and time scales of 2.5 days, possibly corresponding to Rossby–Haurwitz waves (Hendon and Wheeler 2008). In other regions of the spectrum, we see that $\langle\Phi\rangle$ is nearly always less than a tenth of the magnitude of $\langle m\rangle$. The ratio also decreases with increasing wavenumber. Overall, $\mathcal{R}(\langle\Phi\rangle, \langle m\rangle)$ is smaller in ERA5 data than in the DYNAMO data, but still within the expected scaling values suggested by Eq. (37).

c. Accuracy of the MSE budget in the MJO

Last, we examine the amplitudes of $\partial_t\langle m\rangle$, $\partial_t\langle\Phi\rangle$, and $\partial_t K$ in the evolution of the MJO events that occurred during the DYNAMO field campaign. We performed a lag regression of

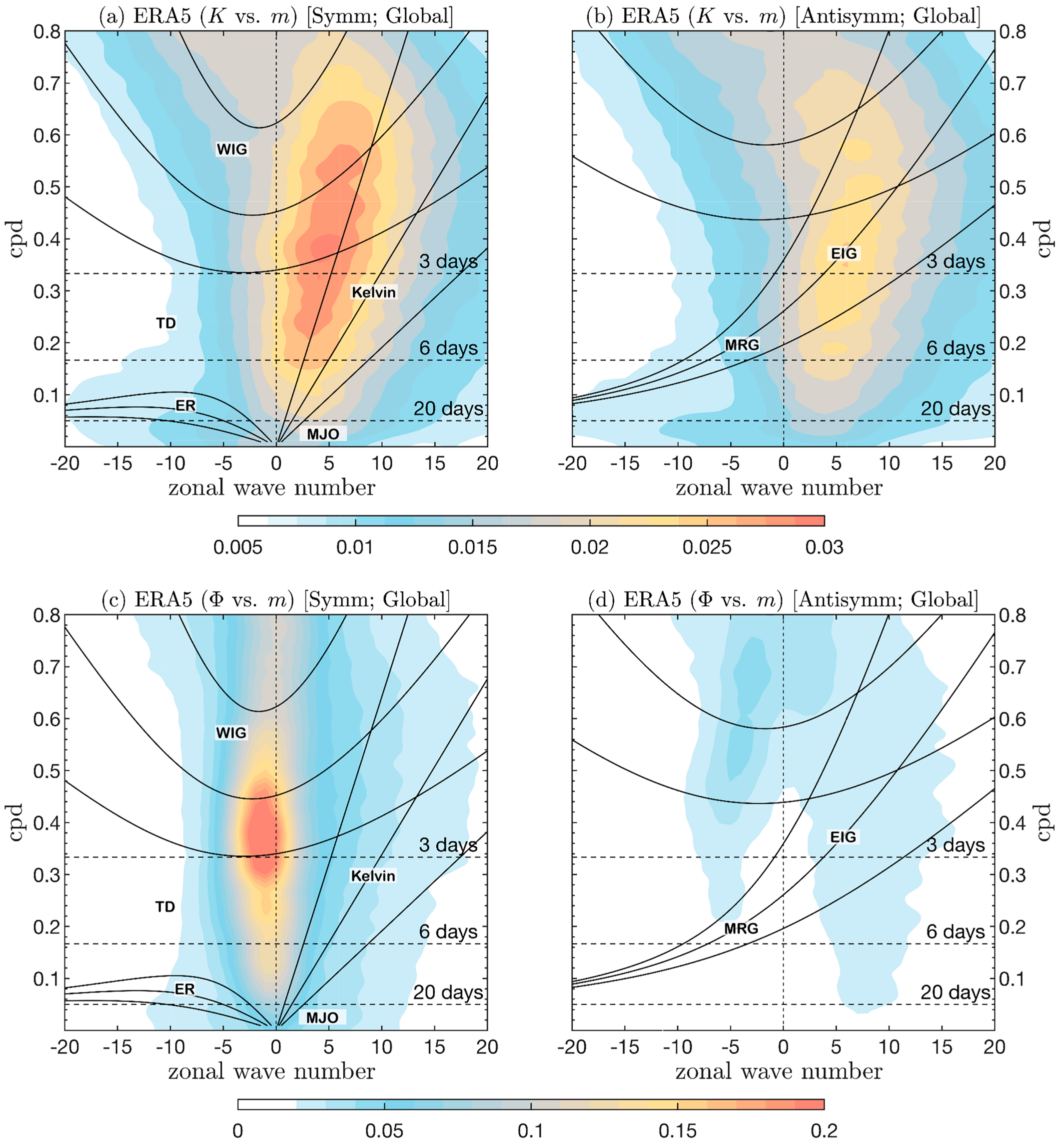

FIG. 2. (a),(b) The square root ratio of the power spectra $\mathcal{R}(\langle K' \rangle, \langle m' \rangle)$ and (c),(d) the $\mathcal{R}(\langle \Phi' \rangle, \langle m' \rangle)$ for the (left) symmetric and (right) antisymmetric components averaged over the 10°S–10°N latitude belt. The dispersion curves correspond to equatorial waves from Matsuno (1966) (each wave is labeled) with equivalent depths of 8, 25, and 90 m. Note that the shading interval in (a) and (b) is different than in (c) and (d).

the sounding data on the first principal component of the OMI index as in Snide et al. (2021). The results, shown in Fig. 3, show that the MSE tendency peaks near 20 W m^{-2}. The tendencies in $\langle \Phi \rangle$ and $\langle K \rangle$ are so small that they are barely discernible in Fig. 3. A close inspection of the two terms (not shown) reveals that $\partial_t \langle \Phi \rangle$ has a peak amplitude of ~0.8 W m^{-2}, 4% the magnitude of $\partial_t \langle m \rangle$. The term $\partial_t \langle K \rangle$ peaks at ~0.2 W m^{-2}, only 1% the magnitude of $\partial_t \langle m \rangle$. The term F_K is even smaller than $\partial_t \langle K \rangle$, and cannot be distinguished from a horizontal line in Fig. 3. The smallness of these three terms is consistent with Eq. (37).

Let us now compare these results with those of the scale analysis. Mayta and Adames Corraliza (2023) found that the value of N$_{\mathrm{mode}}$ for the MJO over the Indian Ocean is ~0.2. According to the scaling in Eq. (37), $\partial_t \langle \Phi \rangle$ should be 6.7% the magnitude of the MSE tendency. If we assume that $U \sim c_p$, then $\partial_t \langle K \rangle$ should be 3.3% the magnitude of the MSE tendency.

5. Discussion and conclusions

In this study, we use a scale analysis, data from ERA5, and sounding data from the DYNAMO northern sounding array to examine the accuracy of the MSE budget. Our results show that the budget is most accurate when a nondimensional parameter N$_{\mathrm{mode}}$ has a small value, implying that the MSE

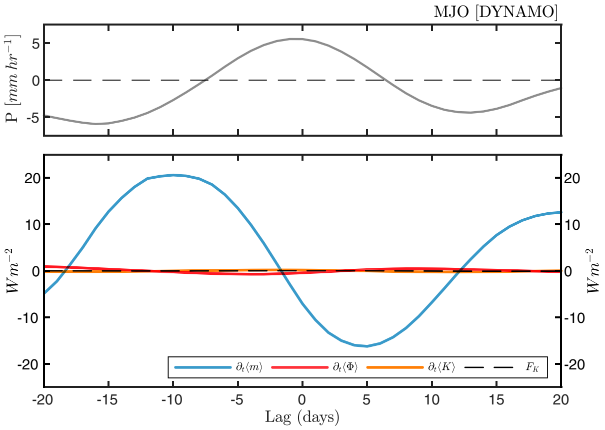

FIG. 3. Time series of (top) precipitation and (bottom) $\partial_t\langle m\rangle$ (blue), $\partial_t\langle\Phi\rangle$ (red), $\partial_t K$ (orange), and F_K (black dashed lines) from DYNAMO data from the northern sounding array. In both panels, the data are lag regressed onto the first principal component of the OMI from lag day −20 to day 20.

budget is most accurate when moisture plays a dominant role in the MSE budget. Additionally, the horizontal winds need to be relatively weak and the surface kinetic energy flux small. These three criteria are most likely to be satisfied in tropical motions with propagation speeds and horizontal winds of 10 m s^{-1} or less. It is also accurate when considering climatological-mean circulations such as the Hadley cell, the ITCZ, and the storm track since $N_{mode} \simeq 0$ in these cases. The scale analysis indicates that the MSE budget is less accurate in systems with strong horizontal winds such as tropical cyclones, as Ma et al. (2015) also noted. It is also likely to be less accurate in fast-propagating systems such as inertio-gravity waves.

Spectral analysis of the conditions necessary to obtain the MSE budget in Eq. (2) from Eq. (15) suggests that the neglected terms are smaller than what the scale analysis suggests. Thus, even though the neglected terms become larger with increasing N_{mode}, the neglected terms rarely exceed ~10% of the tendency. A linear regression analysis of the MJO events that occurred during the DYNAMO field campaign also shows that the conditions described in Eq. (37) are easily satisfied in the MJO. Thus, our results show that the MSE budget as defined in Eq. (2) is reasonably accurate when applied in the context of large-scale systems as long as Eq. (37) is qualitatively satisfied. Fortuitously, most of the applications of the MSE budget in the tropics have been to systems that satisfy Eq. (2), such as the MJO, equatorial Rossby waves, and monsoon low pressure systems (Maloney 2009; Andersen and Kuang 2012; Kim et al. 2014; Mayta et al. 2022; Gonzalez and Jiang 2019; Adames and Ming 2018).

When all these results are considered together, we can find a potential explanation as to why Eq. (2) appears to be widely applicable in the tropics. When the atmosphere is in WTG balance, the ratio c_{ph}^2/c^2 is much smaller than unity (Adames 2022). Mayta and Adames (2023) and Mayta and Adames Corraliza (2023) have shown that c_{ph}^2/c^2 governs the magnitude of N_{mode}. Furthermore, since slowly evolving convectively coupled systems tend to be in thermal wind balance in addition to WTG balance, it follows that the kinetic energy must remain much smaller than the MSE (see Table 4 in Adames 2022). The smallness of N_{mode} and the kinetic energy facilitates the satisfaction of Eq. (37). Thus, we posit that the accuracy of Eq. (2) is largely a result of WTG balance being upheld throughout the tropics.

In spite of these results, we still recommend that readers examine the conditions in Eq. (37) prior to the application of an MSE budget, especially in faster-propagating systems or systems with strong horizontal winds.

Acknowledgments. ÁFAC was supported by NSF CAREER Grant 2236433, and by the University of Wisconsin startup package. The authors thank Spencer Hill and two anonymous reviewers for comments that significantly improved the contents of the manuscript.

Data availability statement. ERA5 data are available at https://www.ecmwf.int/en/forecasts/datasets/reanalysis-datasets/era5/). The DYNAMO data used in this study are available at http://johnson.atmos.colostate.edu/dynamo/products/array_averages/.

APPENDIX A

Derivation of the Column-Integrated E_m Budget

To obtain Eq. (18) we invoke mass continuity [Eq. (3c)] to convert the MSE advection into the MSE flux divergence:

$$\mathbf{u}\cdot\nabla m = \nabla\cdot(\mathbf{u}m), \tag{A1}$$

where $\mathbf{u} = \mathbf{v} + \omega\mathbf{k}$. If $\omega = 0$ at $p = 0$ and at p_s, then column integration of Eq. (A1) eliminates the vertical MSE flux term. We can switch the order of the horizontal divergence operator and the vertical integration, leading to

$$\langle\nabla\cdot(\mathbf{u}m)\rangle = \nabla_h\cdot\langle\mathbf{v}m\rangle. \tag{A2}$$

We must also integrate the two turbulent flux terms, which we will group together. The column integral of the eddy flux divergences is equal to the eddy fluxes evaluated at $p = 0$ and p_s. Assuming that there are no fluxes at $p = 0$, the column integration simplifies to an evaluation at the surface:

$$\frac{1}{g}\int_0^{p_s}\frac{\partial}{\partial p}(\overline{\omega' m'} + \mathbf{v}\cdot\overline{\omega'\mathbf{v}'})dp = -\frac{1}{g}(\overline{\omega' m'} + \mathbf{v}\cdot\overline{\omega'\mathbf{v}'})_s. \tag{A3}$$

The first term on the rhs is the sum of the surface latent and sensible heat fluxes:

$$-\frac{(\overline{\omega' m'})_s}{g} = L_v E + H, \tag{A4}$$

while the term $(\overline{\omega'\mathbf{v}'})_s$ can be evaluated using the bulk aerodynamic formula (Bister and Emanuel 1998; Emanuel 2003):

$$\frac{\mathbf{v}_s\cdot(\overline{\omega'\mathbf{v}'})_s}{g} \simeq \mathbf{v}_s\cdot C_d\rho_s|\mathbf{v}_s|\mathbf{v}_s = C_d\rho_s|\mathbf{v}_s|^3. \tag{A5}$$

Using Eqs. (A1)–(A5) we can obtain Eq. (18).

APPENDIX B

DSE Budget

The DSE budget is often written as

$$\frac{Ds}{Dt} = Q_1. \tag{B1}$$

This equation is an approximation of a more general DSE equation that we write in its column-integrated form as

$$\frac{\partial\langle s + K\rangle}{\partial t} = \frac{\partial\langle\Phi\rangle}{\partial t} - \nabla_h\cdot\langle\mathbf{v}(s + K)\rangle + \langle Q_r\rangle + L_vP - F_K. \tag{B2}$$

To examine whether Eq. (B1) is a good approximation of Eq. (B2), Fig. B1 is as in Fig. 1 but comparing the amplitude of F_K and the tendencies in $\langle\Phi\rangle$ and $\langle K\rangle$ relative to the column DSE tendency. We see that $\partial_t\langle K\rangle$ is an order of magnitude smaller than the DSE tendency at time scales of ~30 days, and diminishes to nearly two orders of magnitude at time scales of 2 days and shorter. The geopotential fluctuations, on the other hand, are 0.2–0.3 times the amplitude of the DSE tendency at all frequencies. The term F_K is the smallest and exhibits a distribution across frequencies that is very similar to that shown in Fig. 1. Based on the results of Fig. B1, we can neglect terms associated with ∂_tK and F_K from Eq. (B2), but not $\partial_t\langle\Phi\rangle$. An accurate approximation of Eq. (B2) is

$$C_p\frac{\partial\langle T\rangle}{\partial t} \simeq -\nabla_h\cdot\langle\mathbf{v}s\rangle + L_vP + \langle Q_r\rangle + H. \tag{B3}$$

The conventional DSE budget in Eq. (B1) is not recommended to use in large-scale motions due to the significant residual that adding $\partial_t\langle\Phi\rangle$ can bring to the budget.

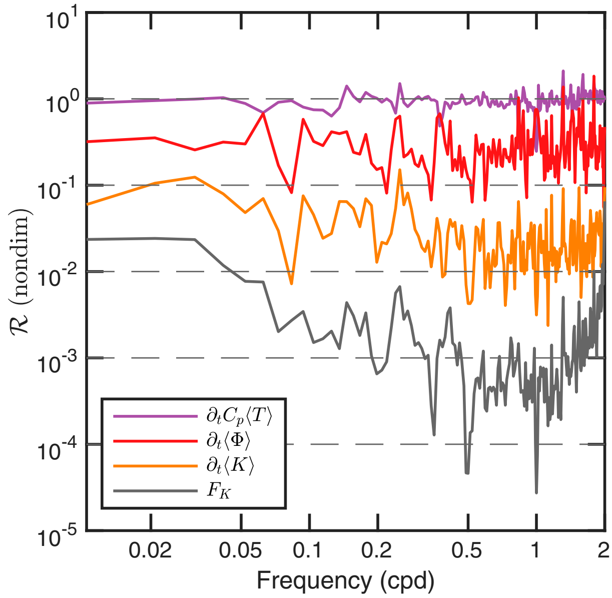

FIG. B1. As in Fig. 1, but showing $\mathcal{R}(C_p\partial_t\langle T\rangle, \partial_t\langle s\rangle)$ (purple), $\mathcal{R}(\partial_t\langle\Phi\rangle, \partial_t\langle s\rangle)$ (red), $\mathcal{R}(\partial_t\langle K\rangle, \partial_t\langle s\rangle)$ (orange), and $\mathcal{R}(F_K, \partial_t\langle s\rangle)$ (gray).

APPENDIX C

Equivalence Between Energy and Column Moist Enthalpy

The column-integrated moist enthalpy h is equivalent to the sum of column-integrated internal, potential, and latent energies:

$$\langle h\rangle = \langle\mathcal{E}\rangle, \tag{C1}$$

where, following the notation of Hill et al. (2017) and Smyth and Ming (2020),

$$\mathcal{E} = C_vT + \Phi + L_vq, \tag{C2}$$

where C_v is the specific heat of air at constant volume. We can verify this identity by following Lorenz (1955) and using integration by parts to show that the mass-weighted integral of Φ is equivalent to the vertical integral of pressure:

$$\int_0^{p_s} z\,dp = \int_0^{p_s} d(pz) + \int_0^{\infty} p\,dz = \int_0^{\infty} p\,dz, \tag{C3}$$

where we note that the integral of $d(pz)$ vanishes since $z = 0$ at the surface and $p = 0$ at the top of the atmosphere. By invoking the ideal gas law $p = \rho R_dT$, we obtain that

$$\langle\Phi\rangle = \int_0^{\infty}\rho R_dT\,dz = R_d\langle T\rangle. \tag{C4}$$

We can then use Eq. (C4) to verify the identity in Eq. (C1).

APPENDIX D

Geostrophic Scaling

We can scale the main variables as in the main text, but using geostrophic scaling rather than equatorial scaling. In this case, geopotential and temperature scales as

$$\Phi = fUL\hat{\Phi}T = \frac{fUL_x}{R_d}\hat{T}. \tag{D1}$$

Other variables scale in the same way. With this definition, $\mathrm{N_{mode}}$ takes the following form:

$$\mathrm{N_{mode}} \equiv \frac{\mathrm{L}_y^2}{\mathrm{L}_d^2\hat{\alpha}(1 - \hat{\alpha})}, \tag{D2}$$

where

$$\mathrm{L}_d = \frac{c}{f} \tag{D3}$$

is the Rossby radius of deformation.

REFERENCES

Adames, Á. F., 2022: The basic equations under weak temperature gradient balance: Formulation, scaling, and types of convectively coupled motions. *J. Atmos. Sci.*, **79**, 2087–2108, https://doi.org/10.1175/JAS-D-21-0215.1.

——, and Y. Ming, 2018: Moisture and moist static energy budgets of South Asian monsoon low pressure systems in GFDL AM4.0. *J. Atmos. Sci.*, **75**, 2107–2123, https://doi.org/10.1175/JAS-D-17-0309.1.

——, and E. D. Maloney, 2021: Moisture mode theory's contribution to advances in our understanding of the Madden-Julian oscillation and other tropical disturbances. *Curr. Climate Change Rep.*, **7**, 72–85, https://doi.org/10.1007/s40641-021-00172-4.

——, D. Kim, S. K. Clark, Y. Ming, and K. Inoue, 2019: Scale analysis of moist thermodynamics in a simple model and the relationship between moisture modes and gravity waves. *J. Atmos. Sci.*, **76**, 3863–3881, https://doi.org/10.1175/JAS-D-19-0121.1.

——, S. W. Powell, F. Ahmed, V. C. Mayta, and J. D. Neelin, 2021: Tropical precipitation evolution in a buoyancy-budget framework. *J. Atmos. Sci.*, **78**, 509–528, https://doi.org/10.1175/JAS-D-20-0074.1.

Andersen, J. A., and Z. Kuang, 2012: Moist static energy budget of MJO-like disturbances in the atmosphere of a zonally symmetric aquaplanet. *J. Climate*, **25**, 2782–2804, https://doi.org/10.1175/JCLI-D-11-00168.1.

Arakawa, A., and W. H. Schubert, 1974: Interaction of a cumulus cloud ensemble with the large-scale environment, Part I. *J. Atmos. Sci.*, **31**, 674–701, https://doi.org/10.1175/1520-0469(1974)031<0674:IOACCE>2.0.CO;2.

Back, L. E., and C. S. Bretherton, 2005: The relationship between wind speed and precipitation in the Pacific ITCZ. *J. Climate*, **18**, 4317–4328, https://doi.org/10.1175/JCLI3519.1.

Barpanda, P., and T. Shaw, 2017: Using the moist static energy budget to understand storm-track shifts across a range of time scales. *J. Atmos. Sci.*, **74**, 2427–2446, https://doi.org/10.1175/JAS-D-17-0022.1.

Benedict, J. J., E. D. Maloney, A. H. Sobel, and D. M. W. Frierson, 2014: Gross moist stability and MJO simulation skill in three full-physics GCMs. *J. Atmos. Sci.*, **71**, 3327–3349, https://doi.org/10.1175/JAS-D-13-0240.1.

Betts, A. K., 1974: Further comments on "A comparison of the equivalent potential temperature and the static energy." *J. Atmos. Sci.*, **31**, 1713–1715, https://doi.org/10.1175/1520-0469(1974)031<1713:FCOCOT>2.0.CO;2.

Bischoff, T., and T. Schneider, 2014: Energetic constraints on the position of the intertropical convergence zone. *J. Climate*, **27**, 4937–4951, https://doi.org/10.1175/JCLI-D-13-00650.1.

Bister, M., and K. A. Emanuel, 1998: Dissipative heating and hurricane intensity. *Meteor. Atmos. Phys.*, **65**, 233–240, https://doi.org/10.1007/BF01030791.

Bretherton, C. S., P. N. Blossey, and M. Khairoutdinov, 2005: An energy-balance analysis of deep convective self-aggregation above uniform SST. *J. Atmos. Sci.*, **62**, 4273–4292, https://doi.org/10.1175/JAS3614.1.

Byrne, M. P., and T. Schneider, 2016: Energetic constraints on the width of the intertropical convergence zone. *J. Climate*, **29**, 4709–4721, https://doi.org/10.1175/JCLI-D-15-0767.1.

Charney, J. G., 1963: A note on large-scale motions in the tropics. *J. Atmos. Sci.*, **20**, 607–609, https://doi.org/10.1175/1520-0469(1963)020<0607:ANOLSM>2.0.CO;2.

Chikira, M., 2014: Eastward-propagating intraseasonal oscillation represented by Chikira–Sugiyama cumulus parameterization. Part II: Understanding moisture variation under weak temperature gradient balance. *J. Atmos. Sci.*, **71**, 615–639, https://doi.org/10.1175/JAS-D-13-038.1.

Ciesielski, P. E., and Coauthors, 2014: Quality-controlled upper-air sounding dataset for DYNAMO/CINDY/AMIE: Development and corrections. *J. Atmos. Oceanic Technol.*, **31**, 741–764, https://doi.org/10.1175/JTECH-D-13-00165.1.

Emanuel, K. A., 1994: *Atmospheric Convection*. Oxford University Press, 580 pp.

——, 2003: Tropical cyclones. *Annu. Rev. Earth Planet. Sci.*, **31**, 75–104, https://doi.org/10.1146/annurev.earth.31.100901.141259.

——, J. D. Neelin, and C. S. Bretherton, 1994: On large-scale circulations in convecting atmospheres. *Quart. J. Roy. Meteor. Soc.*, **120**, 1111–1143, https://doi.org/10.1002/qj.49712051902.

Fuchs, Z., and D. J. Raymond, 2005: Large-scale modes in a rotating atmosphere with radiative–convective instability and WISHE. *J. Atmos. Sci.*, **62**, 4084–4094, https://doi.org/10.1175/JAS3582.1.

Gonzalez, A. O., and X. Jiang, 2019: Distinct propagation characteristics of intraseasonal variability over the tropical west Pacific. *J. Geophys. Res. Atmos.*, **124**, 5332–5351, https://doi.org/10.1029/2018JD029884.

Hendon, H. H., and M. C. Wheeler, 2008: Some space–time spectral analyses of tropical convection and planetary-scale waves. *J. Atmos. Sci.*, **65**, 2936–2948, https://doi.org/10.1175/2008JAS2675.1.

Hersbach, H., and Coauthors, 2019: Global reanalysis: Goodbye ERA-Interim, hello ERA5. *ECMWF Newsletter*, No. 159, ECMWF, Reading, United Kingdom, 17–24, https://doi.org/10.21957/vf291hehd7.

Hill, S. A., Y. Ming, I. M. Held, and M. Zhao, 2017: A moist static energy budget-based analysis of the Sahel rainfall response to uniform oceanic warming. *J. Climate*, **30**, 5637–5660, https://doi.org/10.1175/JCLI-D-16-0785.1.

Huffman, G. J., and Coauthors, 2007: The TRMM Multisatellite Precipitation Analysis (TMPA): Quasi-global, multiyear, combined-sensor precipitation estimates at fine scales. *J. Hydrometeor.*, **8**, 38–55, https://doi.org/10.1175/JHM560.1.

Inoue, K., and L. Back, 2015: Column-integrated moist static energy budget analysis on various time scales during TOGA COARE. *J. Atmos. Sci.*, **72**, 1856–1871, https://doi.org/10.1175/JAS-D-14-0249.1.

——, and ——, 2017: Gross moist stability analysis: Assessment of satellite-based products in the GMS plane. *J. Atmos. Sci.*, **74**, 1819–1837, https://doi.org/10.1175/JAS-D-16-0218.1.

——, Á. F. Adames, and K. Yasunaga, 2020: Vertical velocity profiles in convectively coupled equatorial waves and MJO: New diagnoses of vertical velocity profiles in the wavenumber–frequency domain. *J. Atmos. Sci.*, **77**, 2139–2162, https://doi.org/10.1175/JAS-D-19-0209.1.

Janiga, M. A., and C. D. Thorncroft, 2013: Regional differences in the kinematic and thermodynamic structure of African easterly waves. *Quart. J. Roy. Meteor. Soc.*, **139**, 1598–1614, https://doi.org/10.1002/qj.2047.

——, and C. Zhang, 2016: MJO moisture budget during DYNAMO in a cloud-resolving model. *J. Atmos. Sci.*, **73**, 2257–2278, https://doi.org/10.1175/JAS-D-14-0379.1.

Jiang, X., Á. F. Adames, M. Zhao, D. Waliser, and E. Maloney, 2018: A unified moisture mode framework for seasonality of the Madden–Julian oscillation. *J. Climate*, **31**, 4215–4224, https://doi.org/10.1175/JCLI-D-17-0671.1.

Kiladis, G. N., C. D. Thorncroft, and N. M. J. Hall, 2006: Three-dimensional structure and dynamics of African easterly waves. Part I: Observations. *J. Atmos. Sci.*, **63**, 2212–2230, https://doi.org/10.1175/JAS3741.1.

——, J. Dias, K. H. Straub, M. C. Wheeler, S. N. Tulich, K. Kikuchi, K. M. Weickmann, and M. J. Ventrice, 2014: A comparison of OLR and circulation-based indices for tracking the MJO. *Mon. Wea. Rev.*, **142**, 1697–1715, https://doi.org/10.1175/MWR-D-13-00301.1.

Kim, D., J.-S. Kug, and A. H. Sobel, 2014: Propagating versus nonpropagating Madden–Julian oscillation events. *J. Climate*, **27**, 111–125, https://doi.org/10.1175/JCLI-D-13-00084.1.

LeMone, M. A., G. M. Barnes, and E. J. Zipser, 1984: Momentum flux by lines of cumulonimbus over the tropical oceans. *J. Atmos. Sci.*, **41**, 1914–1932, https://doi.org/10.1175/1520-0469(1984)041<1914:MFBLOC>2.0.CO;2.

Lorenz, E. N., 1955: Available potential energy and the maintenance of the general circulation. *Tellus*, **7**, 157–167, https://doi.org/10.3402/tellusa.v7i2.8796.

Ma, Z., J. Fei, X. Huang, and X. Cheng, 2015: A potential problem with the application of moist static energy in tropical cyclone studies. *J. Atmos. Sci.*, **72**, 3009–3019, https://doi.org/10.1175/JAS-D-14-0367.1.

Madden, R. A., and F. E. Robitaille, 1970: A comparison of the equivalent potential temperature and the static energy. *J. Atmos. Sci.*, **27**, 327–329, https://doi.org/10.1175/1520-0469(1970)027<0327:ACOTEP>2.0.CO;2.

Maloney, E. D., 2009: The moist static energy budget of a composite tropical intraseasonal oscillation in a climate model. *J. Climate*, **22**, 711–729, https://doi.org/10.1175/2008JCLI2542.1.

Marquet, P., 2016: Comments on "MSE minus CAPE is the true conserved variable for an adiabatically lifted parcel." *J. Atmos. Sci.*, **73**, 2565–2575, https://doi.org/10.1175/JAS-D-15-0299.1.

Matsuno, T., 1966: Quasi-geostrophic motions in the equatorial area. *J. Meteor. Soc. Japan*, **44**, 25–43, https://doi.org/10.2151/jmsj1965.44.1_25.

Mayta, V. C., and Á. F. Adames, 2023: Moist thermodynamics of convectively coupled waves over the Western Hemisphere. *J. Climate*, **36**, 2765–2780, https://doi.org/10.1175/JCLI-D-22-0435.1.

——, and ——, 2023: Is the Madden-Julian oscillation a moisture mode? *Geophys. Res. Lett.*, **50**, e2023GL103002, https://doi.org/10.1029/2023GL103002.

——, ——, and F. Ahmed, 2022: Westward-propagating moisture mode over the tropical Western Hemisphere. *Geophys. Res. Lett.*, **49**, e2022GL097799, https://doi.org/10.1029/2022GL097799.

McBride, J. L., 1981: Observational analysis of tropical cyclone formation. Part III: Budget analysis. *J. Atmos. Sci.*, **38**, 1152–1166, https://doi.org/10.1175/1520-0469(1981)038<1152:OAOTCF>2.0.CO;2.

Moncrieff, M. W., and E. Klinker, 1997: Organized convective systems in the tropical western Pacific as a process in general circulation models: A TOGA COARE case-study. *Quart. J. Roy. Meteor. Soc.*, **123**, 805–827, https://doi.org/10.1002/qj.49712354002.

Nakamura, Y., and Y. N. Takayabu, 2022: Convective couplings with equatorial Rossby waves and equatorial Kelvin waves. Part I: Coupled wave structures. *J. Atmos. Sci.*, **79**, 247–262, https://doi.org/10.1175/JAS-D-21-0080.1.

Neelin, J. D., 2007: Moist dynamics of tropical convection zones in monsoons, teleconnections, and global warming. *The Global Circulation of the Atmosphere*, T. Schneider and A. H. Sobel, Eds., Princeton University Press, 267–301.

——, I. M. Held, and K. H. Cook, 1987: Evaporation–wind feedback and low frequency variability in the tropical atmosphere. *J. Atmos. Sci.*, **44**, 2341–2348, https://doi.org/10.1175/1520-0469(1987)044<2341:EWFALF>2.0.CO;2.

Popp, M., and L. G. Silvers, 2017: Double and single ITCZs with and without clouds. *J. Climate*, **30**, 9147–9166, https://doi.org/10.1175/JCLI-D-17-0062.1.

Randall, D., 2015: *An Introduction to the Global Circulation of the Atmosphere*. Princeton University Press, 456 pp.

Raymond, D. J., 2013: Sources and sinks of entropy in the atmosphere. *J. Adv. Model. Earth Syst.*, **5**, 755–763, https://doi.org/10.1002/jame.20050.

——, S. L. Sessions, A. H. Sobel, and Ž. Fuchs, 2009: The mechanics of gross moist stability. *J. Adv. Model. Earth Syst.*, **1**, 20, https://doi.org/10.3894/JAMES.2009.1.9.

Riehl, H., and J. Malkus, 1958: On the heat balance of the equatorial trough zone. *Geophysica*, **6**, 503–538.

Romps, D. M., 2015: MSE minus CAPE is the true conserved variable for an adiabatically lifted parcel. *J. Atmos. Sci.*, **72**, 3639–3646, https://doi.org/10.1175/JAS-D-15-0054.1.

Rydbeck, A. V., and E. D. Maloney, 2015: On the convective coupling and moisture organization of east Pacific easterly waves. *J. Atmos. Sci.*, **72**, 3850–3870, https://doi.org/10.1175/JAS-D-15-0056.1.

Shaw, T. A., P. Barpanda, and A. Donohoe, 2018: A moist static energy framework for zonal-mean storm-track intensity. *J. Atmos. Sci.*, **75**, 1979–1994, https://doi.org/10.1175/JAS-D-17-0183.1.

Smyth, J. E., and Y. Ming, 2020: Characterizing drying in the South American monsoon onset season with the moist static energy budget. *J. Climate*, **33**, 9735–9748, https://doi.org/10.1175/JCLI-D-20-0217.1.

Snide, C. E., A. F. Adames, S. W. Powell, and V. C. Mayta, 2021: The role of large-scale moistening by adiabatic lifting in the Madden–Julian oscillation convective onset. *J. Climate*, **35**, 269–284, https://doi.org/10.1175/JCLI-D-21-0322.1.

Sobel, A. H., J. Nilsson, and L. M. Polvani, 2001: The weak temperature gradient approximation and balanced tropical moisture waves. *J. Atmos. Sci.*, **58**, 3650–3665, https://doi.org/10.1175/1520-0469(2001)058<3650:TWTGAA>2.0.CO;2.

——, S. Wang, and D. Kim, 2014: Moist static energy budget of the MJO during DYNAMO. *J. Atmos. Sci.*, **71**, 4276–4291, https://doi.org/10.1175/JAS-D-14-0052.1.

Soriano, L. J. R., E. L. G. Díez, and F. D. P. Dávila, 1994: Generalized static energy and its conservation. *J. Atmos. Sci.*, **51**, 3281–3285, https://doi.org/10.1175/1520-0469(1994)051<3281:GSEAIC>2.0.CO;2.

Stull, R., 2006: The atmospheric boundary layer. *Atmospheric Science*, 2nd ed. J. M. Wallace and P. V. Hobbs, Eds., Academic Press, 375–417, https://doi.org/10.1016/B978-0-12-732951-2.50014-4.

Sumi, Y., and H. Masunaga, 2016: A moist static energy budget analysis of quasi-2-day waves using satellite and reanalysis data. *J. Atmos. Sci.*, **73**, 743–759, https://doi.org/10.1175/JAS-D-15-0098.1.

Vargas Martes, R. M., Á. F. Adames Corraliza, and V. C. Mayta, 2023: The role of water vapor and temperature in the thermodynamics of tropical northeast Pacific and African easterly waves. *J. Atmos. Sci.*, https://doi.org/10.1175/JAS-D-22-0177.1, in press.

Wheeler, M., and G. N. Kiladis, 1999: Convectively coupled equatorial waves: Analysis of clouds and temperature in the wavenumber–frequency domain. *J. Atmos. Sci.*, **56**, 374–399, https://doi.org/10.1175/1520-0469(1999)056<0374:CCEWAO>2.0.CO;2.

Wing, A. A., K. Emanuel, C. E. Holloway, and C. Muller, 2017: Convective self-aggregation in numerical simulations: A review. *Shallow Clouds, Water Vapor, Circulation, and Climate Sensitivity*, R. Pincus et al., Eds., Space Sciences Series of ISSI, Vol. 65, Springer, 1–25.

——, and Coauthors, 2019: Moist static energy budget analysis of tropical cyclone intensification in high-resolution climate models. *J. Climate*, **32**, 6071–6095, https://doi.org/10.1175/JCLI-D-18-0599.1.

Wolding, B. O., E. D. Maloney, and M. Branson, 2016: Vertically resolved weak temperature gradient analysis of the Madden-Julian oscillation in SP-CESM. *J. Adv. Model. Earth Syst.*, **8**, 1586–1619, https://doi.org/10.1002/2016MS000724.

Yanai, M., S. Esbensen, and J.-H. Chu, 1973: Determination of bulk properties of tropical cloud clusters from large-scale heat and moisture budgets. *J. Atmos. Sci.*, **30**, 611–627, https://doi.org/10.1175/1520-0469(1973)030<0611:DOBPOT>2.0.CO;2.

Yano, J.-I., and M. Bonazzola, 2009: Scale analysis for large-scale tropical atmospheric dynamics. *J. Atmos. Sci.*, **66**, 159–172, https://doi.org/10.1175/2008JAS2687.1.

——, and M. H. P. Ambaum, 2017: Moist static energy: Definition, reference constants, a conservation law and effects on buoyancy. *Quart. J. Roy. Meteor. Soc.*, **143**, 2727–2734, https://doi.org/10.1002/qj.3121.

Yasunaga, K., S. Yokoi, K. Inoue, and B. E. Mapes, 2019: Space–time spectral analysis of the moist static energy budget equation. *J. Climate*, **32**, 501–529, https://doi.org/10.1175/JCLI-D-18-0334.1.

Yoneyama, K., C. Zhang, and C. N. Long, 2013: Tracking pulses of the Madden–Julian oscillation. *Bull. Amer. Meteor. Soc.*, **94**, 1871–1891, https://doi.org/10.1175/BAMS-D-12-00157.1.